nature materials

SUPPLEMENTARY INFORMATION

DOI: 10.1038/NMAT4465

Activating and optimizing MoS_2 basal planes for hydrogen evolution through the formation of strained sulphur vacancies

Hong Li[1†], Charlie Tsai[2,3†], Ai Leen Koh[4], Lili Cai[1], Alex W. Contryman[5,6], Alex H. Fragapane[5,6], Jiheng Zhao[1], Hyun Soo Han[1], Hari C. Manoharan[5,7], Frank Abild-Pedersen[3], Jens K. Nørskov[2,3*] and Xiaolin Zheng[1*]

[1]Department of Mechanical Engineering, Stanford University, Stanford, California 94305, United States

[23]SUNCAT Center for Interface Science and Catalysis, Department of Chemical Engineering, Stanford University, 450 Serra Mall, Stanford, California 94305, United States

[3]SUNCAT Center for Interface Science and Catalysis, SLAC National Accelerator Laboratory, 2575 Sand Hill Road, Menlo Park, California 94025, United States

[4]Stanford Nanocharacterization Laboratory, Stanford University, California 94305, United States

[5]Stanford Institute for Materials and Energy Sciences, SLAC National Accelerator Laboratory, 2575 Sand Hill Road, Menlo Park, California 94025, United States

[6]Department of Applied Physics, Stanford University, Stanford, California 94305, United States

[7]Department of Physics, Stanford University, Stanford, California 94305, United States

*e-mail: Jens K. Nørskov: norskov@stanford.edu, Xiaolin Zheng: xlzheng@stanford.edu

† These authors contributed equally to this work

Supplementary Figures

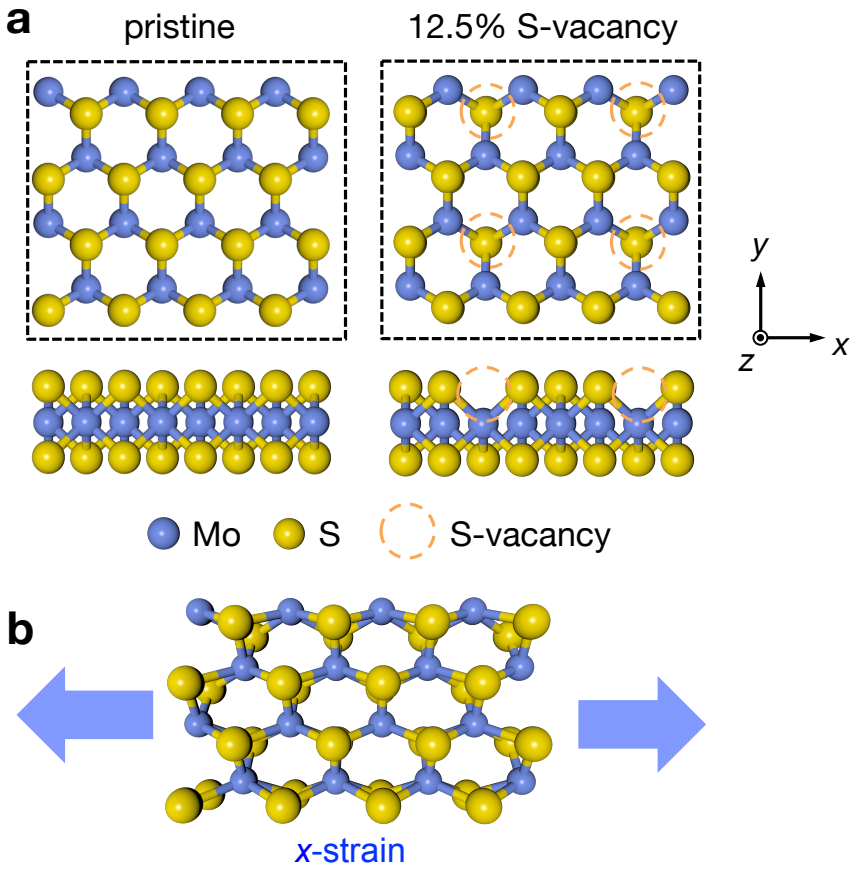

Supplementary Figure S1| Computational unit cell of 2*H*-MoS_2. a, Top view (upper panel) and side view (lower panel) of the atomic structures of the 2*H*-MoS_2 basal plane with 0% (left) and 12.5% S-vacancy (right). Dashed circles label the S-vacancy sites. Inset: the (*x*, *y*, *z*) coordinates. **b,** The schematic of MoS_2 under uniaxial strain in the *x*-direction (*x*-strain). The arrows indicate the directions of elastic strain.

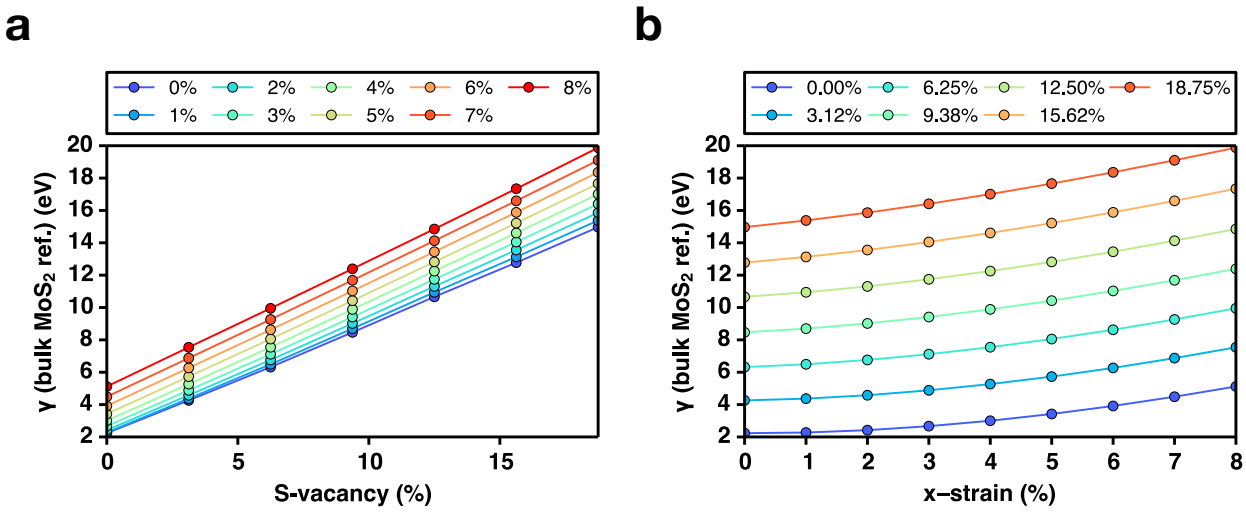

Supplementary Figure S2| Vacancy and strain-dependent stability of MoS_2. The surface energy γ (*w.r.t.* bulk MoS_2) per unit cell versus **a**, %S-vacancy at various uniaxial strains from 0 to 8%, and **b**, uniaxial x-strain with S-vacancy ranging from 0 to 18.75%.

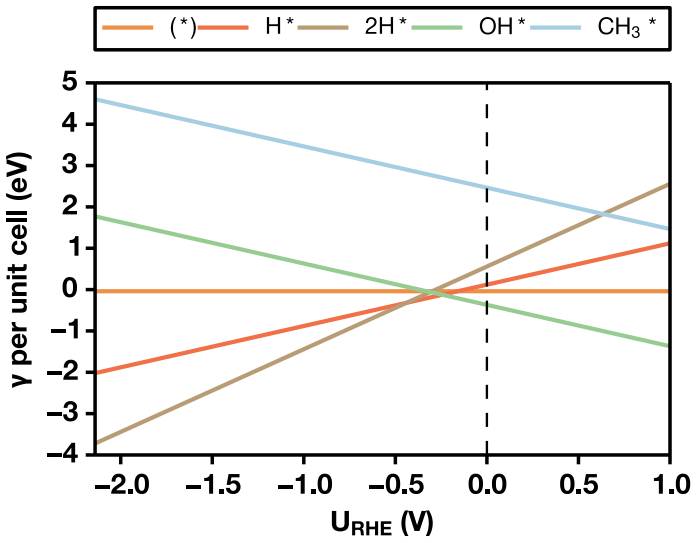

Supplementary Figure S3| Surface energy diagram for adsorbed species on the S-vacancies. Plot of the calculated surface energy (γ) per unit cell as a function of the applied potential versus RHE. An empty S-vacancy site is denoted as (*) and its surface energy γ is set to be 0 eV. Adsorbed species are denoted by *. The thermodynamically preferred surface species is H* under negative potentials and is switched to OH* at near-zero or positive potentials. Dissociated hydrocarbons such as CH_3* are not stable under any operating potentials.

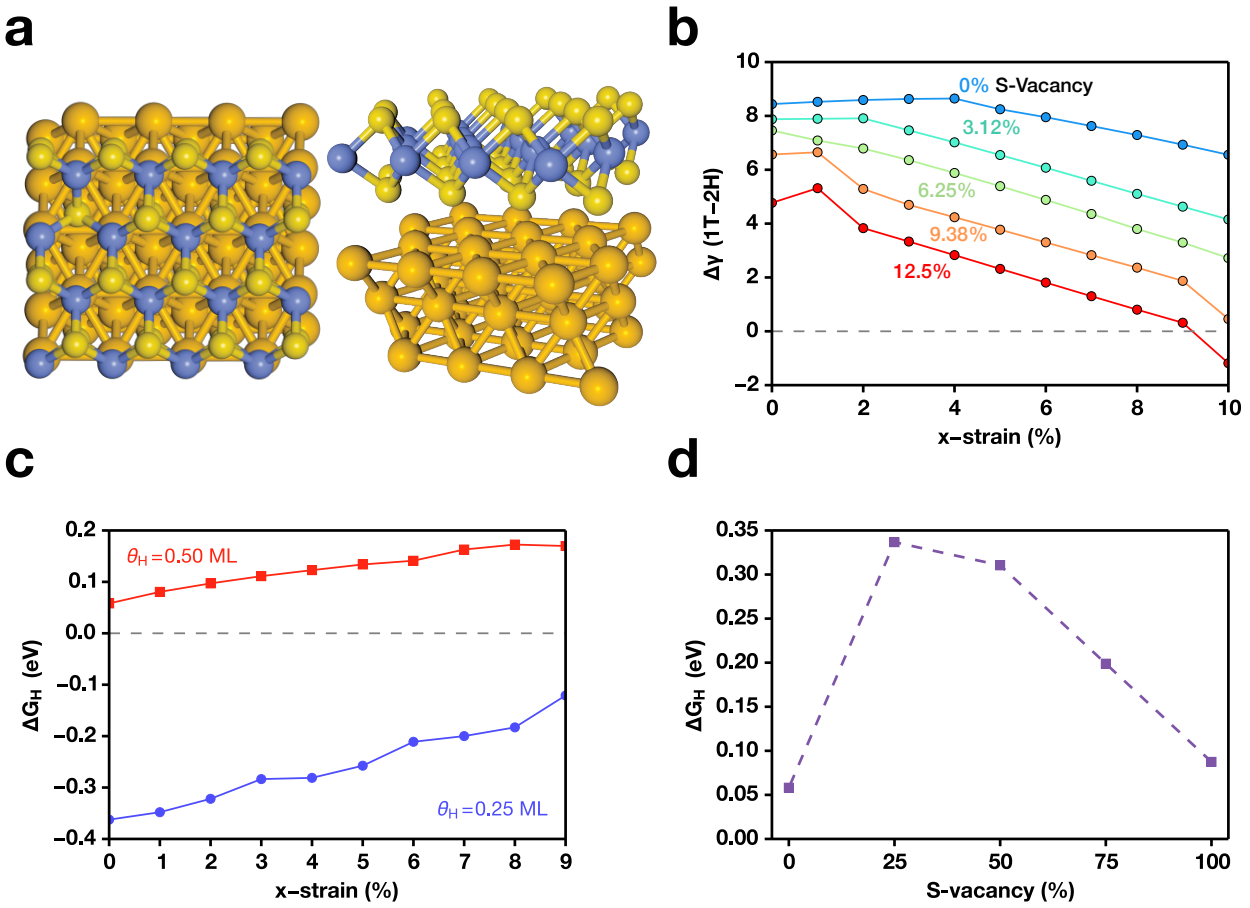

Supplementary Figure S4| Additional factors that could influence the activity of the S-vacancies. a, Top view and angled view of 2*H*-MoS_2 supported on Au(111). The Au(111) support has been strained to match the 2*H*-MoS_2 lattice. **b**, The difference in surface energy between the 1*T*-MoS_2 and the 2*H*-MoS_2 phases as a function of uniaxial x-strain, under a range of S-vacancies from 0% to 12.5%. The $\Delta\gamma$ (1*T*-2*H*) > 0 indicates that the 2*H*-phase is thermodynamically more stable than 1*T*-phase. **c**, Change in ΔG_H on the Mo-edge of 2*H*-MoS_2 due to elastic strain at two relevant hydrogen coverages θ_H of 0.25 ML and 0.50 ML. **d**, Change in ΔG_H on the Mo-edge of 2*H*-MoS_2 due to the formation of S-vacancies.

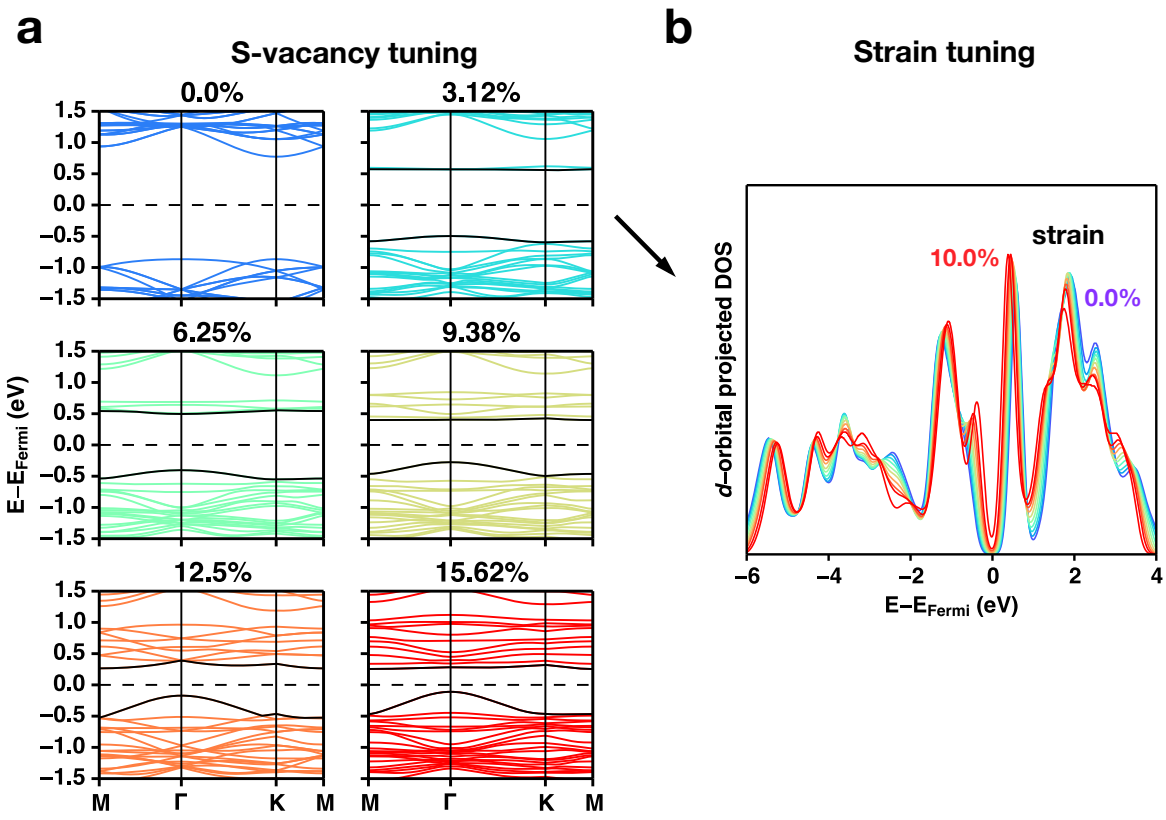

Supplementary Figure S5| Electronic structures of MoS_2 with S-vacancies. a. Evolution of the band structure with increasing S-vacancy concentration (indicated by %). New bands are introduced when S-vacancies are present, and the ones closest to the Fermi level are highlighted in black. **b.** *d*-orbital projected density of states (DOS) where S-vacancy equals 3.12%, showing the effect from strain-tuning. The full 4×4 computational unit cell was used for these calculations.

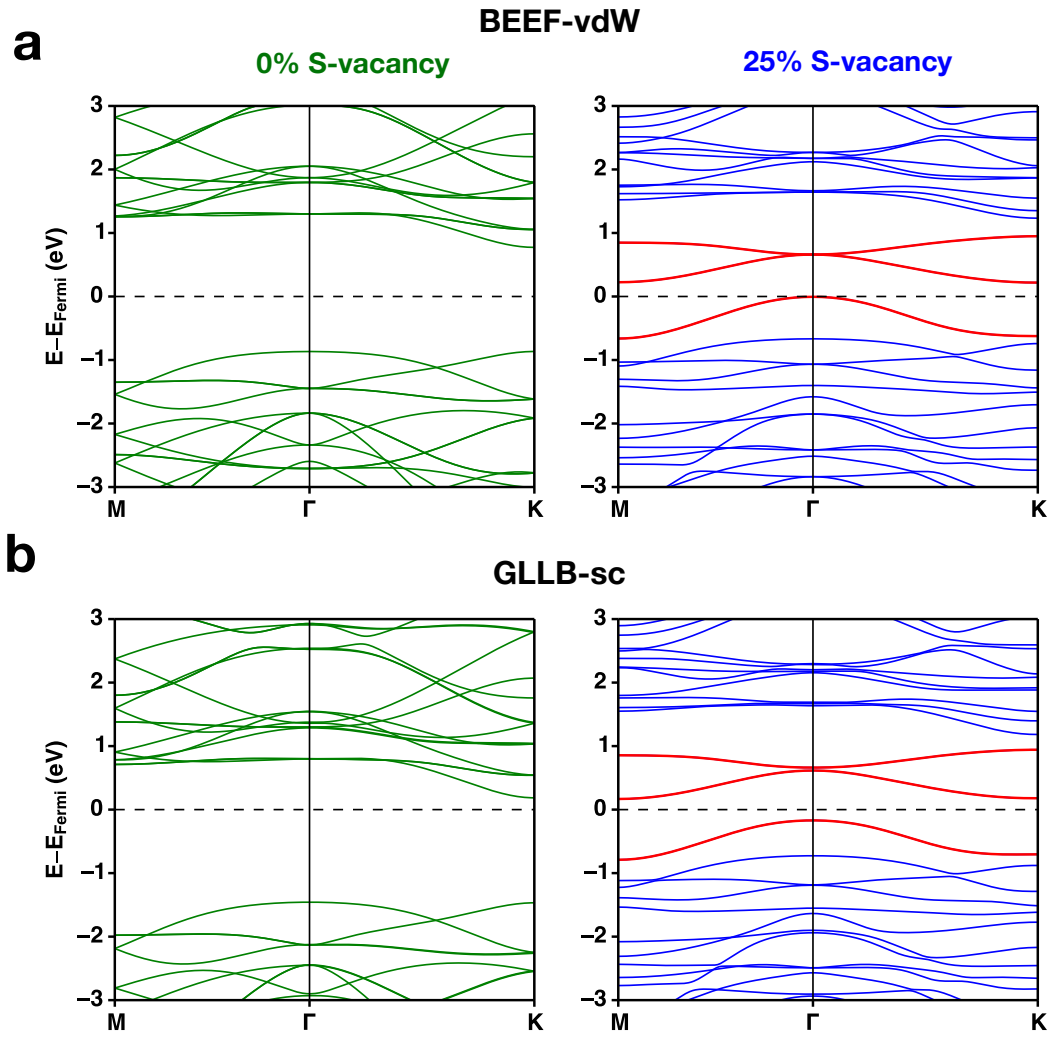

Supplementary Figure S6| Benchmark comparison for band structures. Comparison between the band structures of pristine MoS_2 and MoS_2 with 25% S-vacancies calculated using **a**, BEEF-vdW and **b**, GLLB-sc. New bands associated with the formation of S-vacancies are highlighted in red. The qualitative features are consistent and the band gaps are similar. A reduced 2×2 unit cell was used for these calculations.

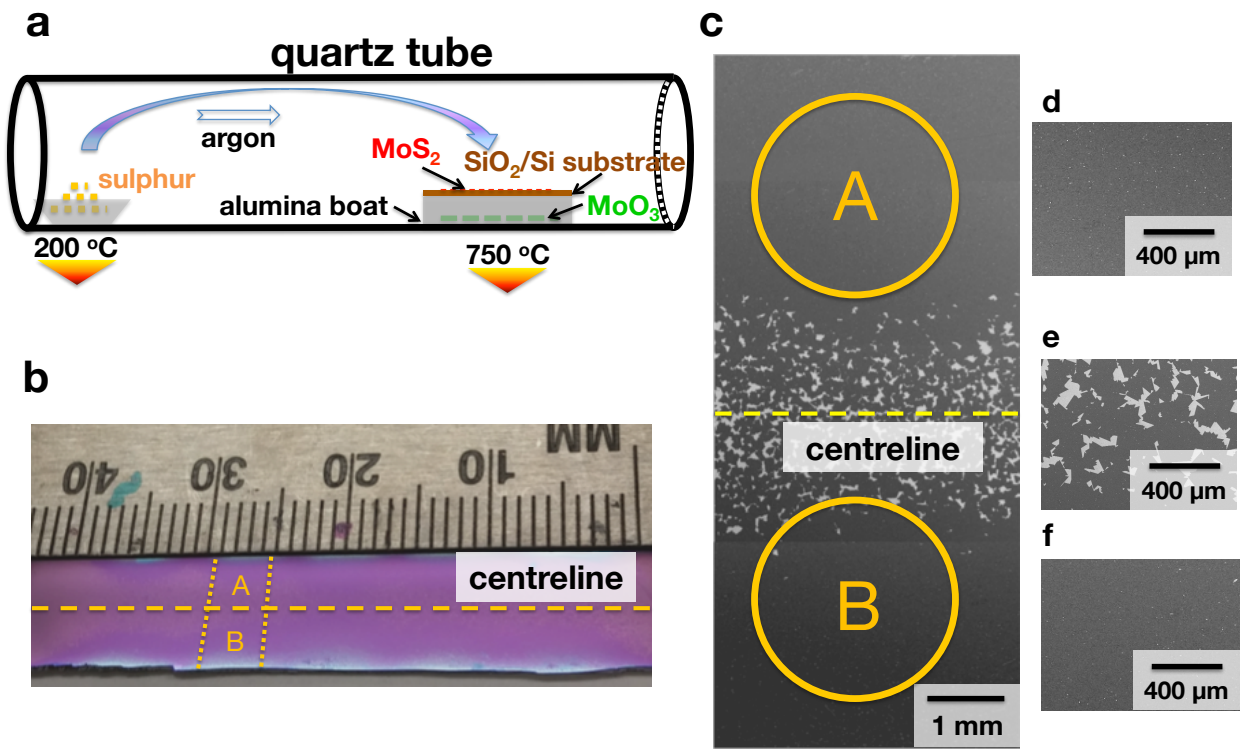

Supplementary Figure S7| Synthesis of continuous MoS_2 monolayer film. a, Schematic of the CVD setup for growing MoS_2. **b**, An optical image of a representative as-grown MoS_2 on a Si/SiO_2 wafer. **c**, A merged SEM image that consists of 4 individual SEM images showing large-area (between the vertical dotted lines in (**b**)) continuous MoS_2 film that is symmetric *w.r.t.* the centreline of the wafer (dashed lines in (**b**) and (**c**)). The circles A and B delineate the areas for HER measurement. The zoomed-in SEM images of the **d**, continuous film in region A, **e**, discrete flakes near the centreline, and **f**, continuous film in region B. The discrete MoS_2 flakes (**e**) show that the average flake size is about 100 ~ 400 μm.

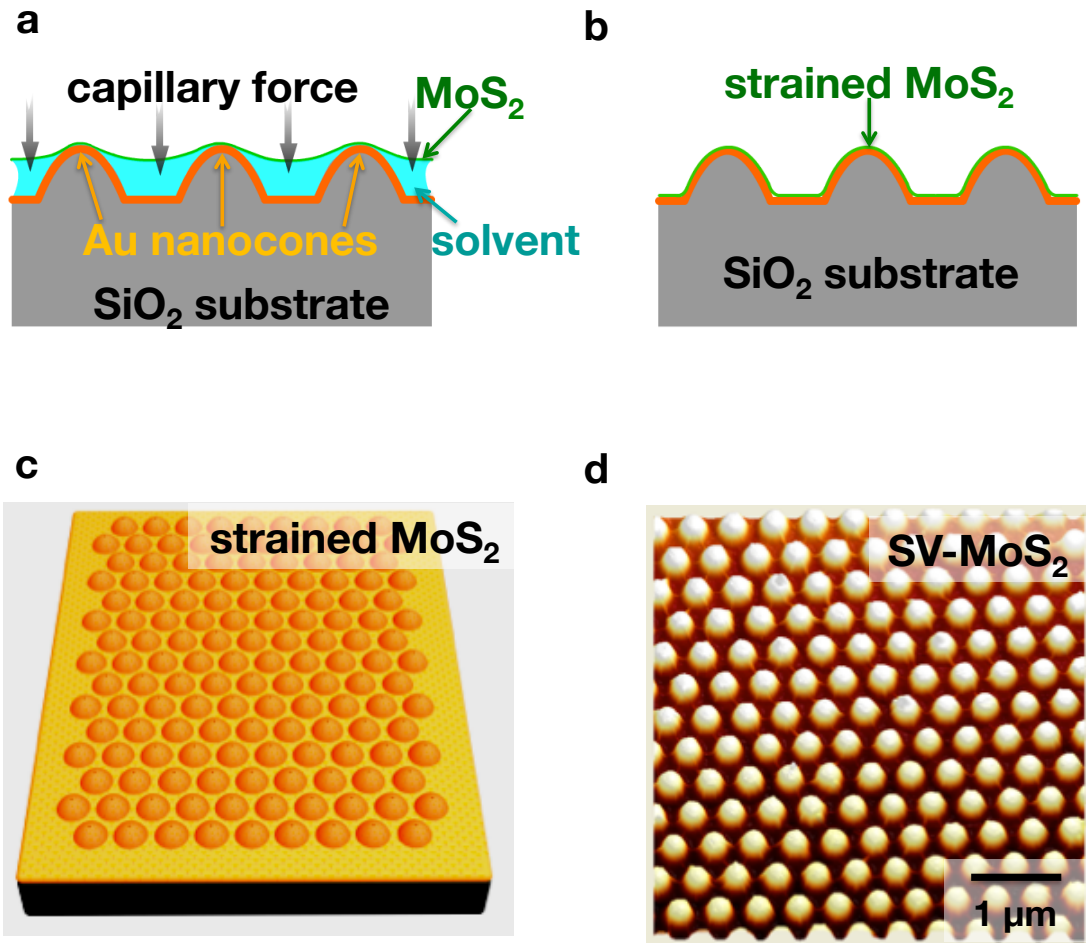

Supplementary Figure S8| Capillary-force induced strain in MoS_2. Schematic side view of **a**, the capillary-force induced straining process of MoS_2 where arrows indicate the direction of capillary force, and **b**, the strained MoS_2 conformally coated on Au nanocones. **c**, Schematic perspective view of strained MoS_2 on a Au nanocone array. **d**, Atomic force microscopy image of strained MoS_2 with S-vacancies (SV-MoS_2) on Au nanocones. Scale bar is 1 μm.

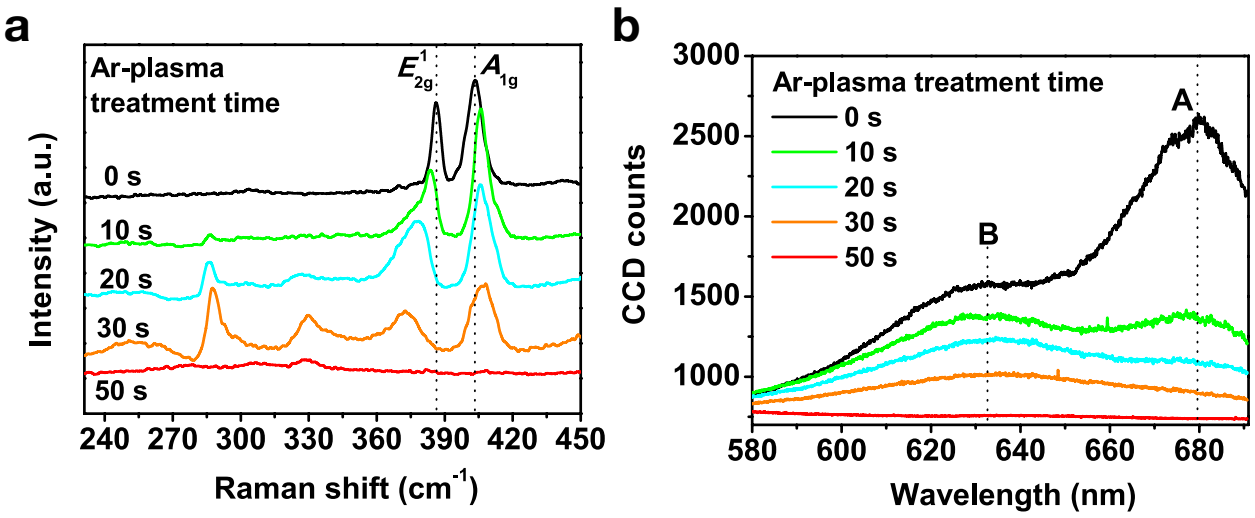

Supplementary Figure S9| Raman and photoluminescence spectroscopy characterizations of MoS_2 with S-vacancies. a, Raman spectra of MoS_2 upon exposure of Ar plasma for 0 (no exposure), 10, 20, 30 and 50 seconds, respectively, from top to bottom. The peaks at 386 and 404 cm^{-1} are assigned to the E^1_{2g} and A_{1g} modes, respectively. **b**, Photoluminescence spectra of MoS_2 upon exposure of Ar plasma for 0 (no exposure), 10, 20, 30 and 50 seconds, respectively, from top to bottom. The peaks at 680 and 633 nm correspond to the A and B exciton peaks, respectively.

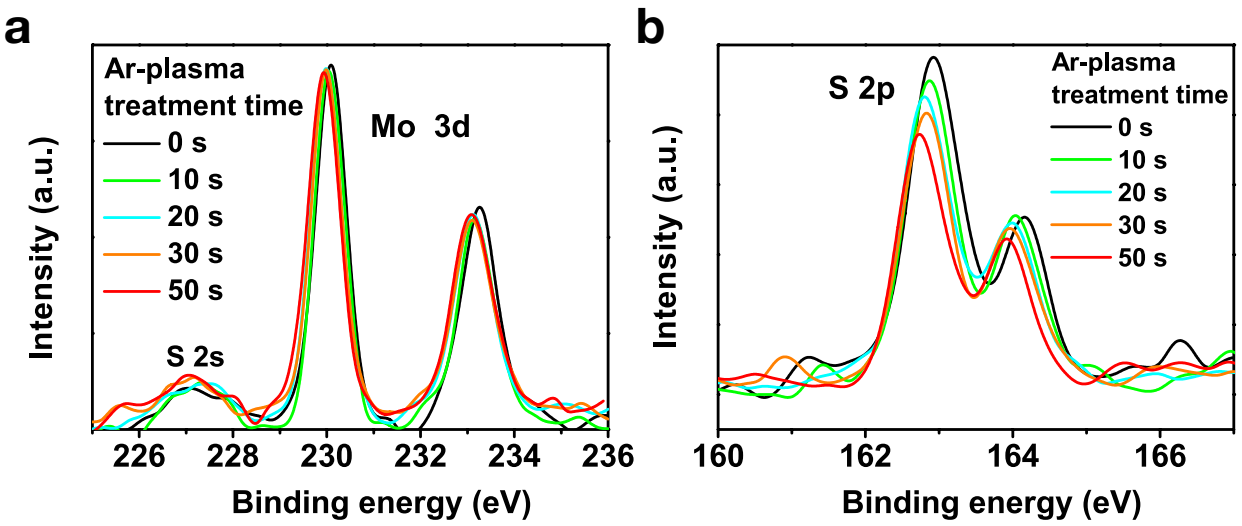

Supplementary Figure S10| X-ray photoelectron spectroscopy characterizations of MoS_2 with S-vacancies. A representative set of X-ray photoelectron spectroscopy spectra of **a**, the Mo 3d states, and **b**, the S 2p state of MoS_2 upon exposure of Ar plasma for 0 (no exposure), 10, 20, 30 and 50 seconds, respectively. The feature of S 2s state are also seen in (**a**) on the left side of Mo 3d peak.

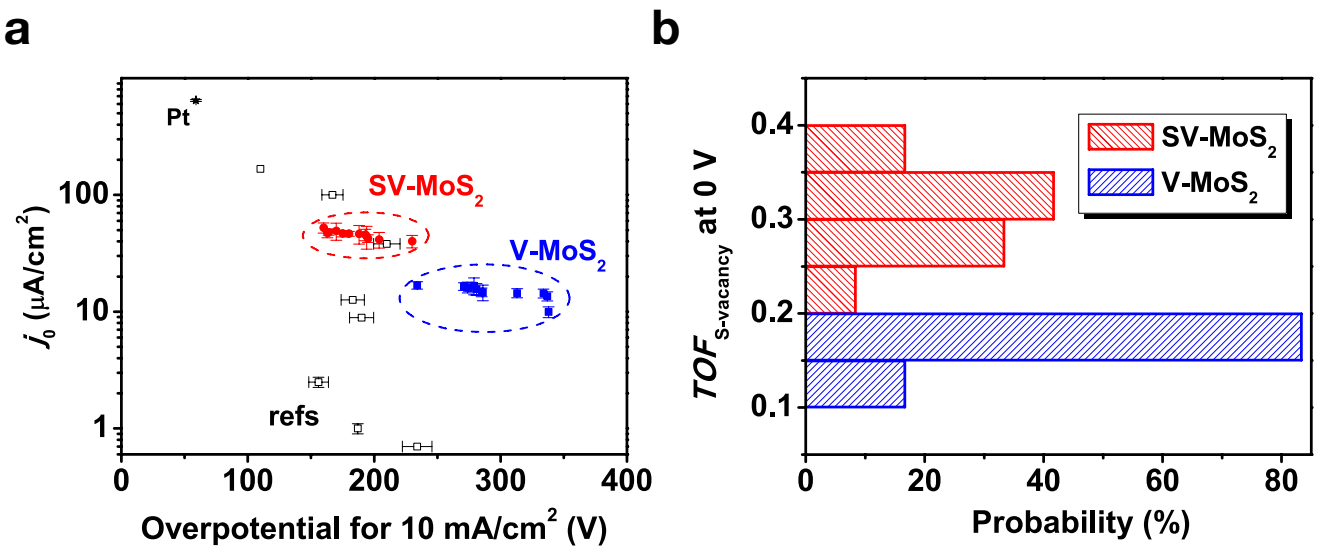

Supplementary Figure S11| Statistical summary of HER activity of MoS_2 with optimal S-vacancy (12.5 ± 2.5%). **a**, Exchange current density j_0 versus overpotential for 10 mA/cm^2, along with reported values (Supplementary refs 1-8). **b**, Distribution of turnover frequency per S-vacancy $TOF_{\text{S-vacancy}}$ at 0 V versus RHE of V-MoS_2 and SV-MoS_2 samples in (**a**).

Supplementary Note 1: Theoretical Approach

Calculation details

All calculations were performed using plane-wave density functional theory (DFT) employing periodic boundary conditions using the Quantum ESPRESSO code[9]. The Bayesian error estimation exchange-correlation functional with van der Waals interactions[10] (BEEF-vdW) was used. This functional has been optimized for chemisorption energies as well as van der Waals interactions, and previous results using both the RPBE and BEEF-vdW functional have been found to be in close agreement[11,12]. A plane-wave cutoff of 500 eV and a density cutoff of 5000 eV were used, and a Monkhorst-Pack[13] 2×2×1 *k*-point grid was used to sample the Brillouin zone. Periodic boundary conditions were used in all directions and 11 Å of vacuum was used in the z-direction to separate the slabs. The convergence criterion for the structural optimizations was a maximum force of 0.05 eV/Å. The lattice parameters were determined to be a = 3.21Å and c = 13.05 Å from previous calculations[12], which were in close agreement with experimental values.

Supplementary Figure S1 shows the computational unit cell (Supplementary Figure S1a) with uniaxial tensile strain along the *x*-axis (Supplementary Figure S1b). Elongating the unit cell in the *x*-direction increased elastic strain correspondingly. In this unit cell size, S-vacancy concentrations in increments of 3.12% (Supplementary Figure S2) are possible, where the S-vacancy % is defined as the total number of S-vacancies divided by the total number of S atoms in the pristine basal plane.

Although standard DFT is known to be poor for estimating the band gap, the GLLB-sc exchange-correlation functional has been shown to be accurate[14,15]. We used the GLLB-sc functional as implemented in the grid-based projector augmented wave code GPAW[16,17], using a 0.15 Å grid spacing. Either the full 4×4 unit cell or a reduced 2×2 unit cell was used to calculate the band structures. The reduced cell was used to obtain a large concentration of S-vacancies in a small unit cell, which simplifies the band structure.

Hydrogen adsorption free energy

The hydrogen adsorption free energies, ΔG_H, were determined in the same way as in previous studies[18,19]. The adsorption energy is defined as

$$\Delta E_H = E(MoS_2{+}H) - E(MoS_2) - \tfrac{1}{2} E(H_2) \quad (1)$$

where (MoS_2+H) refers to hydrogen adsorbed on the MoS_2 surface, (MoS_2) refers to a clean MoS_2 surface, and H_2 refers to gas phase hydrogen molecule. The hydrogen adsorption free energy was calculated at zero potential and pH = 0 as

$$\Delta G_H = \Delta E_H + \Delta E_{ZPE} - T\Delta S \quad (2)$$

where ΔE_H is the hydrogen adsorption energy, ΔE_{ZPE} is the difference in zero point energy, T is the temperature (300 K) and ΔS is the difference in entropy between H that is adsorbed and in the gas phase, at 101325 Pa. A normal mode analysis was used to determine the vibrational frequencies of the adsorbed species, which were used to determine the zero point energy correction and the entropy. The adsorption is too strong if ΔG_H is very negative or too weak if ΔG_H is very positive.

Atomic structures with S-vacancies and strain

Each unit cell consists of 16 Mo atoms and 32 S atoms on the surface. Assuming that S-vacancies are only formed on the surface (top side of the monolayer). With the %S-vacancy being defined as (number of S-vacancies)/(number of total S atoms), this allows us to have increments of 3.125% for one more S-vacancy. Thus having four S-vacancies corresponds to 12.5%. All subsequent S-vacancies from the first one were spaced out as far as possible from existing S-vacancies. To include the effect of strain, the unit cell size was varied *w.r.t.* the optimized lattice parameters. For the range of S-vacancies and strains considered in this work, we observe no noticeable rearrangements in the geometry.

Calculation of stability

Following previous work[20], the surface energies were determined relative to the bulk 2*H*-MoS_2,

$$\gamma = E_{tot} - N_{Mo}E_{bulk}^{MoS_2} + (2N_{Mo} - N_S)\mu_S - N_H\mu_H \quad (3)$$

where E_{tot} is the total energy of the unit cell, N refers to the number of each species in the unit cell, and μ refers to the chemical potential for each species. The surface energy γ is determined per unit cell size. The effect of strain and S-vacancy on the surface energy γ is shown in Supplementary Figure S2. In all cases, increasing strain and S-vacancy raises the surface energy noticeably, and this dependence is more pronounced for the formation of S-vacancies.

Evaluating the possible surface species on the S-vacancies

To determine whether other species could compete with proton adsorption on the S-vacancies of MoS_2, we have constructed a surface energy diagram for the MoS_2 surface with S-vacancies (Supplementary Figure S3). In an aqueous environment, when the applied potential is below –0.24 V versus RHE, the most thermodynamically stable surface species is a single adsorbed hydrogen in the S-vacancy, H* (red line in Figure S3) and then two adsorbed hydrogen atoms at even lower potentials (brown line in Figure S3). When the applied potential is at near-zero or positive potentials, the OH* (green line in Figure S3) and H* covered surfaces are similar in energy (within 0.5 eV of each other) and OH* could compete with H* to adsorb on the S-vacancies sites. For an OH* covered surface, ΔG_H of the H in the OH* was calculated to be 1.18 eV, indicating that the oxygen poisoned S-vacancies are catalytically inert. This is expected, as O* adsorption on the S-vacancy is similar to that of S*, resulting in comparable inertness. Since we observe large increases in the activity, this is further evidence that significant concentrations of OH* are not expected on the surface. We also considered the possibility of hydrocarbon impurities coming from the PMMA process. Hydrocarbon impurities such as CH_4 could dissociatively adsorb into CH_3* and ½ H_2 (g), but they bind more weakly than either OH* or H*. Hence, the S-vacancy sites are expected to be preferentially occupied by H* under our operating conditions.

Influence of the MoS_2-Au substrate interactions on ΔG_H

It is difficult to probe the effect of the MoS_2-Au coupling experimentally, so we have performed DFT calculations to quantify the substrate's effect on the hydrogen binding energy. By using the BEEF-vdW exchange-correlation functional, we are able to accurately describe the van der Waals physisorption of the MoS_2 monolayer as well as the hydrogen chemisorption in the S-vacancy. For the model system, we considered 2*H*-MoS_2 with 3.12% S-vacancies supported on

Au(111) (Supplementary Figure S4a), where the Au(111) slab was strained to match the lattice parameters of 2*H*-MoS_2. We find that ΔG_H in the S-vacancy changes from 0.176 eV (free standing) to 0.151 eV (supported). The difference in ΔG_H is only 0.025 eV, and the true change in ΔG_H due to interactions between Au(111) and 2*H*-MoS_2 is expected to be even smaller since Au(111) becomes more reactive when it is strained[21]. Hence, we expect that the MoS_2-Au substrate coupling would neither alter the trends in the S-vacancy and strain nor modify the requirements for achieving the optimum value of $\Delta G_H = 0$ eV.

Possibility of MoS_2 phase transformations due to S-vacancies and strain

Although we have not observed large distortions in the 2*H*-MoS_2 monolayers either experimentally or theoretically, we still considered if phase transformations from the 2*H*-phase to the 1*T*-phase become more likely due to S-vacancies and applied elastic strain. Using DFT calculations, we find that while both S-vacancies and elastic strain lower the difference in energy between the 1*T*-phase and 2*H*-phase, the 1*T*-phase is still less stable than the 2*H*-phase (Supplementary Figure S4b). Thus, we don't expect phase changes to play a significant role in our system.

Effect of strain and S-vacancies on the edge-sites

In order to minimize the exposure of edge-sites and to focus on the basal plane, we have synthesized and tested large uniform monolayers of 2*H*-MoS_2 in our experiments. However, to further determine the influence of strain and S-vacancies on the edges, DFT calculations were performed for the edges as well. We have used the same computational setups as in previous work[12,18,19]. The Mo-edge has been found to be the relevant edge in HER, where the hydrogen adsorption at a hydrogen coverage (θ_H) of half a H monolayer (ML), $\theta_H = 0.5$ ML is 0.06 eV and is the active species. We determined the change in ΔG_H due to strain at both $\theta_H = 0.5$ ML and a lower coverage of $\theta_H = 0.25$ ML and find that hydrogen adsorption is weakened in both cases (Supplementary Figure S4c). Since at $\theta_H = 0.5$ ML, ΔG_H on the edge-sites is on the weak side without elastic strain, hydrogen adsorption only becomes less favourable when strain is applied. Since the hydrogen at lower coverage ($\theta_H = 0.25$ ML) is on the strong side without elastic strain, the hydrogen binding becomes closer to 0 eV when strain is applied. However, even at 8% strain,

which is far beyond what has been considered in this work, ΔG_H is still further from 0 eV than that of the 0.5 ML case without strain, *i.e.* a completely unstrained edge. Hence, the observed increase in HER activity for our strained MoS_2 could not be due to strained edge-sites. In addition, the effect of S-vacancies on ΔG_H in the edges was also considered (Supplementary Figure S4d), where ΔG_H was worse than the pristine edge for S-vacancy concentrations between 25% (isolated S-vacancy in a unit cell) to 100% (all S-atoms at the edges removed). Any formation of S-vacancies on exposed edges is thus also not expected to contribute to increases in the HER activity.

Electronic structure of the S-vacancy

The evolution of the band structure with increasing S-vacancy concentration is shown in Supplementary Figure S5a. When S-vacancies are introduced, new bands appear above and below the Fermi level. Further increases in the S-vacancy concentration shift these bands towards the Fermi level and thus increase the number of electronic states around the Fermi level. The effect of applying tensile strain is shown in Supplementary Figure S5b, where the density of states (DOS) becomes narrower and the electronic states around the Fermi level increase. These new mid-gap states are also experimentally confirmed by scanning tunnelling microscopy/spectroscopy measurements of MoS_2 with S-vacancies, which is discussed below in Supplementary Note 2.

Comparison between BEEF-vdW and GLLB-sc

Band structure calculations were performed using the BEEF-vdW exchange-correlation functional in order to be consistent with all other calculations in this manuscript. To confirm whether or not the band structures are reasonable, we compared the results with ones that are calculated using the GLLB-sc exchange-correlation functional, which is known to accurately reproduce band gaps for semiconductors. In Supplementary Figure S6, the qualitative features of the BEEF-vdW (Supplementary Figure S6a) and GLLB-sc (Supplementary Figure S6b) band structures are similar, and both band gaps are also similar (~1.7 eV).

Supplementary Note 2: Experimental details

Growth of monolayer 2H-MoS_2 using chemical vapour deposition (CVD) method

Molybdenum trioxide (MoO_3) and sulphur powder were used as the precursors for MoS_2. MoO_3 (< 1 mg) powder was loaded in a ceramic boat. A piece of Si wafer capped with 270-nm-thick SiO_2 layer was suspended on the ceramic boat. Then the ceramic boat was put at the centre of a 1-inch quartz tube furnace. Another ceramic boat containing sulphur powder (~ 1g) was placed upstream (Supplementary Figure S7a). The quartz tube was repeatedly pumped down to 0.01 mbar and subsequently filled with Ar gas (100 sccm) to 1 atm for three times to purge the oxygen molecules in the tube. Then the tube was heated to 400 ºC and the Ar flow rate was set to 6 sccm. Afterward, the sulphur boat was moved to a heating zone that reaches 200 ºC during the growth. The temperature in the centre of the tube was then increased to 750 ºC and maintained at 750 ºC for 15 min. Finally, the system was naturally cooled down to room temperature while in the presence of Ar flow.

As shown in Supplementary Figure S7b, MoS_2 flakes are grown over a large area (~10-mm-wide and 50-mm-long) and the growth is symmetric *w.r.t.* the centreline of the wafer (Supplementary Figure S7c). Raman characterization across the wafer surface shows the majority of the film consists of monolayer MoS_2 (> 90%). The density of MoS_2 flakes decreases gradually from edge to the centreline of the wafer since the MoO_3 vapour concentration is higher at the wafer edges and lower near the centre. The discontinuous MoS_2 flakes near the centreline (Supplementary Figure S7c) have sizes around 100 ~ 400 μm (Supplementary Figure S7e), and the MoS_2 flakes away from the centreline are continuous (Supplementary Figures S7d and S7f). We typically chose the symmetric and continuous regions A and B (Supplementary Figure S7c) for HER experiments. Assuming that connected equilateral-triangle flakes of side length L~100 μm cover the entire area of measurement, the total density of edge-site S atoms is on the order of $\sim 10^{10}$ sites/cm^2, which is only 10^{-4} of the total density of S-vacancy sites ($\sim 10^{14}$ sites/cm^2, see later discussion). We therefore neglect the contribution of edge-sites towards HER activity in our sample. It is worth noting that the mass loadings of these HER electrodes are extremely small (only three atomic layers of S-Mo-S).

Capillary-force induced strain in MoS_2

Monolayer polystyrene nanospheres (diameters ~ 500 nm) were assembled on a Si/SiO_2 (270 nm) wafer by either the spin coating or using the Langmuir-Blodgett method. Afterward, the size of the nanospheres was reduced to 250 nm using oxygen plasma. The nanospheres was used as a mask for the plasma etching of SiO_2 in a mixture of fluoroform and oxygen and then removed by sonication in chloroform. Subsequently, a titanium (10 nm)/gold (80 nm) bilayer was deposited onto the SiO_2 nanocones to form the gold nanocone substrate. The CVD monolayer MoS_2 was coated with 1 μm-thick PMMA, removed from the growth substrate by potassium hydroxide (KOH) etching. After the SiO_2 layer was etched away, the PMMA-MoS_2 film floated on the surface and was carried up using the gold nanocone substrate to complete the transfer. The sample was then baked at 100 °C for 10 min and then subsequently soaked in acetone and chloroform sequentially to remove PMMA completely. Afterward, the sample was soaked in ethylene glycol under vacuum for 1 hour to ensure both sides of MoS_2 membrane were wetted by ethylene glycol. Lastly, the sample was dried in air to evaporate the ethylene glycol completely. The capillary force induced by ethylene glycol evaporation pulls the MoS_2 membrane down to follow the topography of the nanocone surface (see Supplementary Figure S8, more details can be found in our previous work[22]). Tensile strain is thus created in MoS_2.

Transmission electron microscopy (TEM) characterization of MoS_2 with S-vacancies

The as-grown MoS_2 film was transferred to a TEM grid using the same PMMA-assisted transfer method discussed earlier. Then the sample was treated with mild Ar plasma to create S-vacancies. The sample on the TEM grid was characterized with a FEI spherical aberration (image)-corrected 80-300 Titan environmental (scanning) (FEI Titan E-(S)TEM) operated at 80 kV. It is noted that serious line defects[23] can be found when the electron beam exposure time was over 60 s. In order to minimize such knock-on damage, the electron beam exposure time was limited to 20 s for each region of the specimen investigated. We noted that when the Ar-plasma treatment time was increased to 50 s, the film became unstable in TEM and holes were soon formed upon the electron beam exposure.

Raman and photoluminescence (PL) characterization of MoS_2 with S-vacancies

The as-grown MoS_2 film was transferred to a clean SiO_2 wafer using the same PMMA-assisted transfer method. The transferred MoS_2 samples were exposed to mild Ar plasma for various durations. The Raman and PL measurements were performed with the excitation laser line of 532 nm using a WITEC alpha500 Confocal Raman system in ambient air environment. The power of the excitation laser line was kept well below 1 mW to avoid damage of MoS_2. The Raman scattering was collected by an Olympus 100 × objective (N.A. = 0.9) and dispersed by 1800 (for Raman measurements) and 600 (for PL measurements) lines/mm gratings.

The as-transferred MoS_2 shows typical Raman spectra of monolayer MoS_2 that consists of two dominant peaks at 385.9 (E^1_{2g}, the in-plane vibration mode) and 404 cm^{-1}(A_{1g}, the out-of-plane vibration mode), as shown in Supplementary Figure S9a. The difference in frequency is about 18 cm^{-1}, a unique Raman feature of monolayer MoS_2[24]. Upon the formation of S-vacancies, both E^1_{2g} and A_{1g} peaks broadened. This is due to perturbations to the perfect *2H*-phase lattice, resulting in poorly defined vibrational mode energies, suggesting that the creation of vacancies changes the vibrational energies of the lattice. Moreover, red and blue shifts are observed for E^1_{2g} and A_{1g} peaks, respectively. This is caused by changes in the restoring force constant of these vibrational modes due to vacancy formation, providing further evidence that Mo-S bonds have been perturbed by the vacancies. Vacancy formation also causes additional peaks in the Raman spectrum. There is a broad peak between 240 and 260 cm^{-1} that could be related to the physisorption of oxygen molecules on the sulphur vacancies in air[25]. Another additional peak at 287 cm^{-1} is attributed to the E_{1g} mode that is normally not observable for the 2*H*-phase using a back-scattering setup[26], and its presence could be caused by the bond-angle rearrangement. The third additional peak 329 cm^{-1} could arise from the other phase formation locally[8].

The above analysis suggests that there are rearrangements of the Mo-S chemical bonds with increasing amounts of removed S atoms, and even possibly local phase transformations. Nevertheless, E^1_{2g} and A_{1g} peaks are still the strongest on the Raman spectra, indicating the monolayer MoS_2 is still dominantly *2H*-phase.

The evolution of PL spectra is shown in Supplementary Figure S9b. The as-transferred MoS_2 shows two dominant emission peaks A and B, consistent with its monolayer nature. As the

Ar-plasma treatment duration increases, the intensity of the PL emission peak continuously decreases due to changes to the lattice structure, which agrees with previous findings[27]. The PL emission completely disappears when the plasma treatment duration is more than 50 s. These Raman and PL spectra shows that (1) the as-grown MoS_2 is monolayer; (2) atomic bond arrangements change with varying plasma treatment time, resulting in electronic structure changes; and (3) severe atomic rearrangement/reconstruction could occur with prolonged plasma treatment. Most importantly, the gradual evolution of both Raman and PL spectra suggests that the desulfurization process was well controlled.

X-ray photoelectron spectroscopy (XPS) characterization of MoS_2 with S-vacancies

The as-grown MoS_2 film was transferred onto a gold substrate using the same PMMA-assisted transfer method. The transferred MoS_2 film was treated with Ar plasma for various durations to create different concentration of S-vacancies. The XPS measurements were performed at 5×10^{-10} Torr using excitation by Al(ka) radiation. The normalized spectra of the Mo 3d state and S 2p state are shown in Supplementary Figures S10a and S10b. First, the Mo 3d peak remains almost unchanged with different Ar-plasma treatment time, which suggests that Ar plasma has little influence on the Mo atoms, and it is consistent with the absence of Mo vacancy in the TEM image (main Figure 3e). Second, the S 2p peak intensity does decrease with increasing the Ar-plasma treatment time (from top to bottom), indicating the formation of S-vacancy. To quantify the XPS information, we measured the XPS peak area ratio of S 2p to Mo 3d states for as-grown MoS_2 and normalized the value of S:Mo ratio to 2.0, and we use this as a reference to obtain the S:Mo atomic ratios for MoS_2 samples undergoing different Ar-plasma treatment times (main Figure 3f).

Local electronic probe of MoS_2 with S-vacancies using scanning tunnelling microscopy

Scanning tunneling microscopy/spectroscopy (STM/STS) was used to obtain the electronic structure of MoS_2 with S-vacancies directly. The STM/STS measurements were carried out at 77 K in ultrahigh vacuum. A MoS_2 sample with ~12.5% S-vacancies on a gold surface was prepared using the aforementioned process. The STS *dI/dV* was measured directly using a lock-in amplifier and modulating the sample bias at an amplitude of 10 mV. The measurements

were smoothed to remove noise. Figure 3g (main text) shows dI/dV versus the sample bias V, where dI/dV is proportional to the DOS[28]. The large, sharp peak inside the band gap region is attributed to the newly introduced electronic states by S-vacancies. This is in excellent qualitative agreement with the calculated projected *d*-orbital DOS (calculated on a freestanding monolayer) shown in the same figure, which has been shifted by –1.2 eV to account for doping from the Au substrate (red curve in main Figure 3g).

Calculation of the turnover frequency

The turnover frequency is calculated using the current density j and the active site density N according to Supplementary Equation 4,

$$TOF = \frac{\text{Total number of } H_2 \text{ atoms per second}}{\text{Total number of active sites per unit area}} = \frac{j/(2\times q)}{N} \tag{4}$$

where $q = 1.6\times10^{-19}$ C is the elementary charge, and 2 accounts for 2 H atoms per H_2 molecule. To calculate the turnover frequency per surface Mo atom (TOF_{Mo}), the Mo atom density (N_{Mo}) is estimated to be about 1×10^{15} cm^{-2} from the MoS_2 lattice constant ~3.2 Å. To calculate the turnover frequency per S-vacancy site ($TOF_{S\text{-vacancy}}$), the S-vacancy site density is estimated using Supplementary Equation 5,

$$N_{S\text{-vacancy}} = \left(2\times N_{Mo}\right)\times(\%\text{S-vacancy}) \tag{5}$$

where (%S-vacancy) is the atomic S-vacancy percentage out of the total number of S atoms measured by XPS. There is a factor of 2 in Supplementary Equation 5 since we assume that only S atoms on top of monolayer MoS_2 are removed by Ar plasma according to our TEM image (main Figure 3e). This should give an upper bound for the density of S-vacancies and hence the lower bound of $TOF_{S\text{-vacancy}}$. To estimate $TOF_{S\text{-vacancy}}$ at 0 V versus RHE, we used the exchange current density j_0 that was linearly extrapolated from the Tafel plots for j in Supplementary Equation 4.

Supplementary References

1 Xie, J. *et al.* Controllable Disorder Engineering in Oxygen-Incorporated MoS_2 Ultrathin Nanosheets for Efficient Hydrogen Evolution. *J. Am. Chem. Soc.* **135**, 17881-17888 (2013).

2 Li, Y. *et al*. MoS_2 Nanoparticles Grown on Graphene: An Advanced Catalyst for the Hydrogen Evolution Reaction. *J. Am. Chem. Soc.* **133**, 7296-7299 (2011).

3 Shi, J. *et al.* Controllable Growth and Transfer of Monolayer MoS_2 on Au Foils and Its Potential Application in Hydrogen Evolution Reaction. *ACS Nano* **8**, 10196-10204 (2014).

4 Wang, H. *et al.* Electrochemical tuning of vertically aligned MoS_2 nanofilms and its application in improving hydrogen evolution reaction. *Proc. Natl Acad. Sci. USA* **110***,* 19701-19706 (2013).

5 Wang, H. *et al.* Electrochemical Tuning of MoS_2 Nanoparticles on Three-Dimensional Substrate for Efficient Hydrogen Evolution. *ACS Nano* **8**, 4940-4947 (2014).

6 Xie, J. *et al.* Defect-Rich MoS_2 Ultrathin Nanosheets with Additional Active Edge Sites for Enhanced Electrocatalytic Hydrogen Evolution. *Adv. Mater.* **25**, 5807-5813 (2013).

7 Kibsgaard, J., Chen, Z., Reinecke, B. N. & Jaramillo, T. F. Engineering the surface structure of MoS_2 to preferentially expose active edge sites for electrocatalysis. *Nat. Mater.* **11**, 963-969 (2012).

8 Lukowski, M. A. *et al.* Enhanced Hydrogen Evolution Catalysis from Chemically Exfoliated Metallic MoS_2 Nanosheets. *J. Am. Chem. Soc.* **135**, 10274-10277 (2013).

9 Giannozzi, P. *et al.* QUANTUM ESPRESSO: a modular and open-source software project for quantum simulations of materials. *J. Phys. Condens. Matter.* **21**, 395502 (2009).

10 Wellendorff, J. *et al.* Density functionals for surface science: Exchange-correlation model development with Bayesian error estimation. *Phys. Rev. B* **85**, 235149 (2012).

11 Hinnemann, B. *et al.* Biomimetic Hydrogen Evolution: MoS_2 Nanoparticles as Catalyst for Hydrogen Evolution. *J. Am. Chem. Soc.* **127**, 5308-5309 (2005).

12 Tsai, C., Abild-Pedersen, F. & Nørskov, J. K. Tuning the MoS_2 Edge-Site Activity for Hydrogen Evolution via Support Interactions. *Nano Lett.* **14**, 1381-1387 (2014).

13 Monkhorst, H. J. & Pack, J. D. Special points for Brillouin-zone integrations. *Phys. Rev. B* **13**, 5188-5192 (1976).

14 Kuisma, M., Ojanen, J., Enkovaara, J. & Rantala1, T. T. Kohn-Sham potential with discontinuity for band gap materials, *Phys. Rev. B* **82**, 115106 (2010).

15 Castelli, I. E. *et al*. New Light‐Harvesting Materials Using Accurate and Efficient Bandgap Calculations. *Adv. Energy Mater.* **5**, 1400915 (2015).

16 Mortensen, J. J., Hansen, L. B. & Jacobsen, K. W. Real-space grid implementation of the projector augmented wave method. *Phys. Rev. B* **71**, 035109 (2005).

17 Enkovaara, J. *et al*. Electronic structure calculations with GPAW: a real-space implementation of the projector augmented-wave method. *J. Phys.: Condens. Matter*. **22**, 253202 (2010).

18 Tsai, C., Chan, K., Abild-Pedersen, F. & Nørskov, J. K. Active edge sites in $MoSe_2$ and WSe_2 catalysts for the hydrogen evolution reaction: a density functional study. *Phys. Chem. Chem. Phys.* **16**, 13156-13164 (2014).

19 Tsai, C., Chan, K., Abild-Pedersen, F. & Nørskov, J. K. Theoretical Insights into the Hydrogen Evolution Activity of Layered Transition Metal Dichalcogenides. *Surf. Sci.* doi: 10.1016/j.susc.2015.01.019.

20 Bollinger, M. V., Jacobsen, K. W. & Nørskov, J. K. Atomic and electronic structure of MoS_2 naonparticles. *Phys. Rev. B* **67**, 129906 (2003).

21 Mavrikakis, M., Hammer, B. & Nørskov, J. K. Effect of Strain on the Reactivity of Metal Surfaces. *Phys. Rev. Lett.* **81**, 2819-2822 (1998).

22 Li, H. *et al*. Optoelectronic crystal of artificial atoms in strain-textured MoS_2. *Nat. Commun.* 6:7381 doi: 10.1038/ncomms8381.

23 Komsa, H.-P., Kurasch, S., Lehtinen, O., Kaiser, U. & Krasheninnikov, A. From point to extended defects in two-dimensional MoS_2: Evolution of atomic structure under electron irradiation. *Phys. Rev. B* **88**, 035301 (2013).

24 Li, H. *et al.* From Bulk to Monolayer MoS_2: Evolution of Raman Scattering. *Adv. Funct. Mater.* **22**, 1385-1390 (2012).

25 Islam, M. R. *et al.* Tuning the electrical property via defect engineering of single layer MoS_2 by oxygen plasma. *Nanoscale* **6**, 10033-10039 (2014).

26 Wieting, T. J. & Verble, J. L. Infrared and Raman Studies of Long-Wavelength Optical Phonons in Hexagonal MoS_2. *Phys. Rev. B* **3**, 4286-4292 (1971).

27 Quan, M. *et al.* Controlled argon beam-induced desulfurization of monolayer molybdenum disulfide. *J. Phys. Condens. Matter* **25**, 252201 (2013).

28 Tersoff, J. & Lang, N. D. in *Scanning Tunneling Microscopy*, vol. 27 of Methods in Experimental Physics, J. A. Stroscio, W. J. Kaiser (Academic Press, San Diego, 1993), 22-23.